Nanoscale

Accepted Manuscript

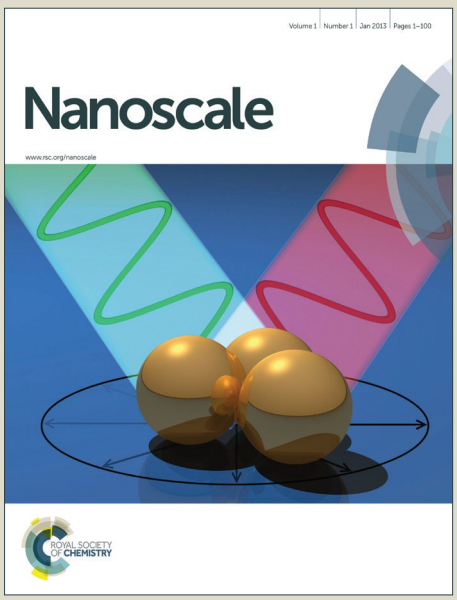

ROYAL SOCIETY OF CHEMISTRY

www.rsc.org/nanoscale

Nanoscale

ARTICLE

Synthesis of Co-based bimetallic nanocrystals with one-dimensional structure for selective control on syngas conversion

Received 00th January 20xx,
Accepted 00th January 20xx

DOI: 10.1039/x0xx00000x

www.rsc.org/

RongbinBa,[a,b] YonghuiZhao,[a] Lujing Yu,[a,b] Jianjun Song,[a,b] Shuangshuang Huang,[a,b] LiangshuZhong,[a] Yuhan Sun,*[a,c] and Yan Zhu*[a,c]

Co-based bimetallic nanocrystals with one-dimensional (1D) branches are synthesized by heterogeneous nucleation of Co atoms onto the prenucleated seeds such Pd or Cu through a facile wet-chemical route. The peripheral branches (rod-like) of Co-Pd and Co-Cu nanocrystals outspread along (001) direction and are enclosed by (101) facets. By switching the prenucleated metals to form robust Co-Pd or Co-Cu bimetallic nanocatalysts, the selectivity of CO hydrogenation could be purposely adjusted towards heavy paraffins, light olefins or oxygenates. The Anderson-Schulz-Flory chain-lengthening probabilities for products are up to 0.9 over Co-Pd nanocrystals, showing that long-chain hydrocarbons can be formed with high selectivity using the targeted design of Co-Pd nanocrystal catalysts. These Co-based bimetallic nanocrystals with 1D structure exhibit superior catalytic activities to the corresponding Co-based nanoparticles for synthesis gas conversion.

Introduction

To control the final products of syngas (synthesis gas) conversion ($CO+H_2$) is of paramount importance with challenge, since the products are too many and product distributions are quite wide and complex.[1-5] Efficient metals such Fe and Co are popular as spherical catalysts used in syngas conversion reaction.[6-10] These spherical catalysts have some difficulties like size polydispersity and heterogeneity of surface structure,[11] even if routine or incremental work competently carried out,[12-14] however no significant advance in the well-defined structure of bimetallic catalysts for syngas conversion is reported in the related literatures. The synthesis of bimetallic nanocrystals with uniform shape and nicely defined composition is inherently more complicated than that of monometallic nanocrystals, due to the difficulty in accessing a predictable condition to induce the homogeneous nucleation and growth of two alien metal ions.[15,16] The high quality bimetallic nanocrystals with well-defined structure and homogeneous composition distribution are still desired. Moreover, it is necessary to explore how novel structure rather than spherical particle of bimetallic catalysts affects the activity, products selectivity and distribution of syngas conversion. Herein drawing lessons from the mechanism of vapor-liquid-solid (VLS) method,[17] our efforts aim at controlling 1D growth of cobalt-based bimetallic nanocrystals such as Co-Pd and Co-Cu via a wet chemical route, and meanwhile studying the effects of noble metal Pd and non-noble metal Cu on catalysis by Co catalyst for syngas conversion.

In this work, to induce the anisotropic growth of Co nanocrystal, the heterogeneous nucleation of Co nanocrystal is carried out onto the surface of prenucleated seeds such Pd or Cu as anchoring points to drive one-sided growth of Co nanocrystal through the intraparticle electrochemical Ostwald-ripening, similar to VLS process. In this way, binary Co-Pd or Co-Cu nanocrystals with peripheral branches growing along (001) direction can be synthesized. In particular, by switching the prenucleated metal from Pd to Cu to form Co-Pd or Co-Cu bimetallic nanocatalysts with rod-like branches, the selectivity of syngas conversion could be controlled efficiently towards heavy hydrocarbons and light oxygenates. Compared with conventional CoPd or CoCu spherical nanoparticles prepared using coprecipitation methods, Co-Pd or Co-Cu nanocrystals with 1D branches could achieve higher catalytic activity of syngas conversion. Especially, Co-Pd nanocrystals with 1D branches favored the carbon chain growth to obtain more heavy hydrocarbons than CoPd nanoparticles, while Co-Cu nanocrystals with 1D branches showed a similar catalytic selectivity to CoCu nanoparticles for syngas conversion, indicating that selectivity of syngas conversion is more sensitive to the structure of CoPd catalysts than one of CoCu.

Experimental Section

Synthesis of Co-Pd nanocrystals with 1D structure

0.75 g of $Co(OAc)_2{\cdot}4H_2O$ and 1.065 g of stearic acid were added into 70 mL of propylene glycol to form solution A. After solution A was stirred for 30 min, appropriate amount of $Pd(NO_3)_2{\cdot}2H_2O$ was dissolved into 40 mL of 1,2-propanediol and stirred for 10 min until it turned black (solution B). Solution B was injected into solution A

[a] CAS key laboratory of Low-Carbon Conversion Science and Engineering, Shanghai Advanced Research Institute, Chinese Academy of Sciences, Shanghai 201210, China. E-mail: zhuy@sari.ac.cn; sunyh@sari.ac.cn
[b] University of Chinese Academy of Sciences, Beijing 100049, China.
[c] School of Physical Science and Technology, ShanghaiTech University, Shanghai 201210, China.

Electronic Supplementary Information (ESI) available: [details of any supplementary information available should be included here]. See DOI: 10.1039/x0xx00000x

by a pipettor. The mixture was stirred for 5 min and then transferred into a Teflon-lined autoclave (100 mL) and maintained at 190 ^{o}C for 5 h. The product obtained was separated by a magnet, thoroughly washed with ethanol, and finally dried at 60 ^{o}C for 4 h under vacuum.

Synthesis of Co-Cu nanocrystals with 1D structure

0.75 g of $Co(OAc)_2{\cdot}4H_2O$ and 1.065 g of stearic acid and 1.05 g hexadecylamine were dissolved into 70 mL of propylene glycol to form solution A. After solution A was stirred for 30 min, appropriate amount of $Cu(OAc)_2{\cdot}H_2O$ was dissolved into 10 mL of 1,2-propanediol and stirred for 30 min in the water bath at 60 ^{o}C (solution B). Solution B was injected into solution A. The mixture was stirred for 5 min and then transferred into a 100 mL Teflon-lined autoclave and maintained at 160 ^{o}C for 15 h. The product obtained was separated by a magnet, thoroughly washed with ethanol, and finally dried at 60 ^{o}C for 4 h under vacuum.

Catalytic test of CO hydrogenation

CO hydrogenation reaction was carried out in a fixed bed micro-reactor. Prior to the reaction, the catalyst samples (2 g, 40~60 mesh) were activated in 10% H_2/N_2 flow of 6000 mL/(g·h), the reduction temperature was programmed to rise from room temperature to 573 K and to maintain at that temperature for 2 h, and then to cool down to the desired temperature for the catalyst test. The syngas with a molar ratio of $H_2/CO/N_2$ = 65/32/3 was gradually introduced to the catalyst. The reaction was conducted with gas flow rate of 3000 mL/(g·h) and the gas flow was controlled by a calibrated Brooks mass flow controller. The pressure was gradually raised to 6 MPa, and then the temperature was slowly increased to the desired temperature. Analysis of H_2, CO, CO_2, and CH_4 was performed using a packed TDX-01 column and a thermal conductivity detector. Gaseous hydrocarbons (C_1-C_8) were separated in a capillary Poraplot Q column and analyzed by a flame-ionization detector. The aqueous products were analyzed offline by GC, which was equipped with dual detectors (TCD and FID) and dual Porapak Q columns. The oil products were separated in a HP-1 column and analyzed by a flame-ionization detector. The wax products, which were dissolved in CS_2, were analyzed using a MXT-1 column and a flame-ionization detector. All the data were collected after 24 h on-stream when the steady state was reached. The mass balance, carbon balance and oxygen balance were calculated at each product collecting time, and kept between 95 % and 105 %.

Characterization

X-ray diffraction (XRD) patterns of samples were recorded on a Japanese Rigaku Ultima IV powder diffractometer using Cu Kα radiation with the wavelength of 1.54056 Å at 40 kV and 40 mA. Rietveld refinement with MDI-Jade software was used to determine the lattice constants from the XRD diffraction analysis. The morphology and size of nanomaterials were characterized using JEOL JEM-2100 Electron Microscope (JEOL, TEM, 2011, Japan) operated at 200 kV and S4800 of Hitachi. The X-ray Photoelectron Spectroscopy (XPS) of the samples were determined on a RBD upgraded PHI-5000C ESCA System in a high-vacuum chamber with the base pressure below 1×10^{-8} Torr. Products from syngas conversion were analyzed by Shimadzu GC-2014 with dual detectors (TCD and FID) and different columns. The chemical element analysis was determined by ICP (Optima 8000). The specific surface areas of the catalysts were calculated from N_2 adsorption isotherms using the BET and BJH methods (ASAP 2010).

Results and Discussion

Figure 1a displays a representative scanning electron microscopy (SEM) image of Co-Pd nanocrystals (denoted as $CoPd_{0.001}$, where the weight percent content of Pd in $CoPd_{0.001}$ is 0.1%). The nanocrystal is viewed as core-shell geometry, and the core is solid with 100 nm size and the shell is constructed with nanorods (20 nm diameter, 400 nm length), which are observed from transmission electron microscopy (Figure 1b). The growth direction of the nanorods is along (001), which is obtained by the lattice spacing of 0.19 nm indicating the (101) planes of hexagonal-packed Co phase (inset of Figure 1b), and the other inset of figure 1b is the fast Fourier-transform pattern also confirming that the peripheral nanorods outspread along the (001) direction. $CoPd_{0.0005}$ (0.05 wt% Pd) and $CoPd_{0.01}$ (1 wt% Pd) nanocrystals also have 3D core-shell structure, shown in Figure 1c-d and corresponding the insets. The energy-dispersive X-ray spectroscopy (EDS) mapping analysis (Figure 1e-h) clearly points to the distribution ranges of Co (red) and Pd (green) in the $CoPd_{0.01}$ nanocrystals, revealing a bimetallic structure. Without metal seeds at the beginning, Co nanocrystals with peripheral rod-like structure were not obtained (Figure S1). Here, the higher electronegativity of Pd caused Pd^{2+} ions to be first reduced by propylene glycol (served as the solvent and reductant) to form neutral Pd atoms. Positive Co^{2+} ions attracted the electron cloud of the Pd atoms and the Pd atoms were polarized towards Co^{2+} center. The continuous supply of electrons from propylene glycol to Pd (Pd as an acceptor, reducing agent as a donator) made electron density shift from Pd to Co until the formation of Co-Pd nucleation, and subsequently Co-Pd nucleation grew up towards Co-Pd nanocrystal. A series of experimental conditions were carried out to gain deeper insight into how the 3D core-shell structure of Co-Pd formed (see Supporting Information and corresponding Figure S1-4).

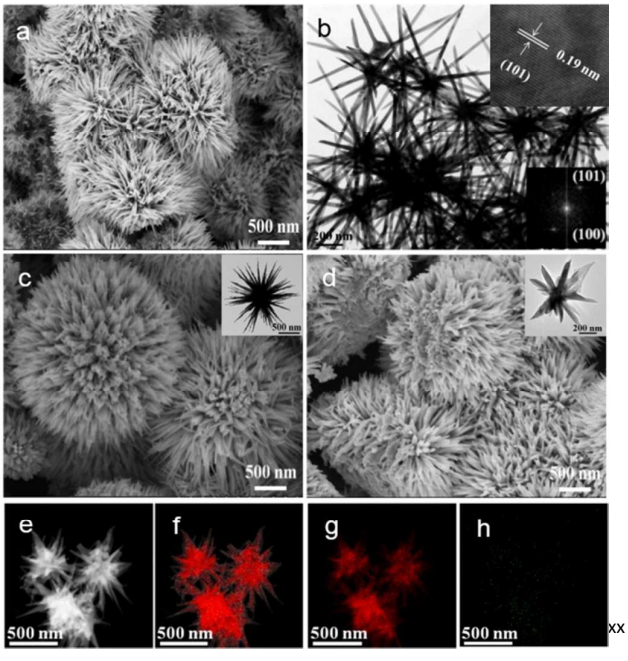

Figure 1. (a) SEM image of $CoPd_{0.001}$. (b) TEM image of $CoPd_{0.001}$, and insets are HRTEM image of $CoPd_{0.001}$ and a fast Fourier transform (FFT) analysis from HRTEM. (c) SEM image of $CoPd_{0.0005}$ and inset is TEM image of $CoPd_{0.0005}$. (d) SEM image of $CoPd_{0.01}$ and insets is TEM image of $CoPd_{0.01}$. (e) Bright-field TEM image of $CoPd_{0.01}$ and (f-h) the corresponding element maps of Co (red) and Pd (green) in $CoPd_{0.01}$ nanocrystals.

Reversible switch of selective control on syngas conversion can be accomplished by Cu replacing Pd as prenucleated seeds to form Co-Cu nanocrystals, since CuCo catalysts favor the insertion of non-dissociative adsorbed CO into intermediate carbon species to form oxygenates.[18-20] Figure 2a-d reveal the Co-Cu nanocrystals with 1D branches including $CoCu_{0.01}$ (1 wt% Cu), $CoCu_{0.05}$ (5 wt% Cu), $CoCu_{0.1}$ (10 wt% Cu) and $CoCu_{0.2}$ (20 wt% Cu). Exact elemental analysis of Co-Cu nanocrystals (and Co-Pd) is indicated by Inductively coupling plasma (ICP) spectroscopy (Table S1). Note that the length of rod-like branches of $CoCu_{0.01}$ is up to micrometer scale. The length of peripheral branches of $CoCu_{0.05}$ is about 400 nm, which is similar to that of $CoCu_{0.1}$ but longer than that of $CoCu_{0.2}$ (200 nm). The cores of the four Co-Cu samples are similar about size of 100 nm. Interestingly, the distribution of Cu in the Co-Cu nanocrystals takes on a different look, compared to that of Pd in Co-Pd nanocrystals. The concentration of Cu in the kernel is obvious higher than that of the peripheral branches, which is observed from the element maps of Cu (red) and Co (green) in $CoCu_{0.01}$ (Figure 2e-h). It also identifies the homogenous distribution of Cu and Co in 1D branches of Co-Cu nanocrystals. The control experiments with Co-Cu nanocrystals are depicted in Supporting Information and corresponding results are shown in Figure S5.

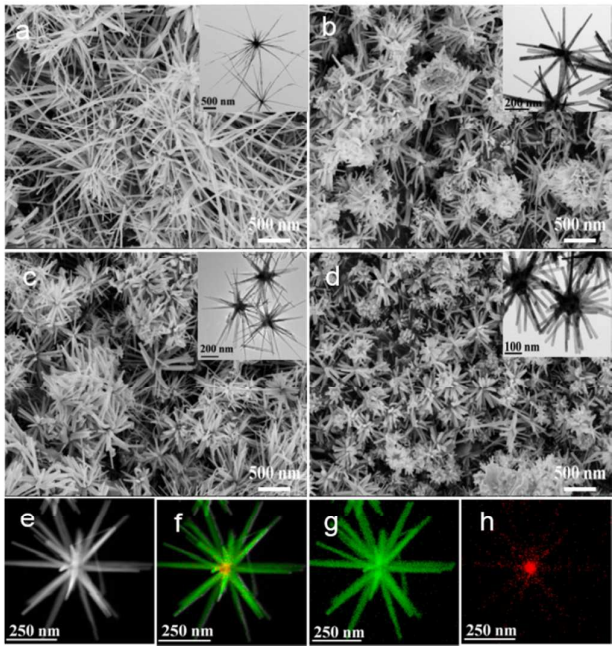

Figure 2. SEM images of (a) $CoCu_{0.01}$, (b) $CoCu_{0.05}$, (c) $CoCu_{0.1}$ and (d) $CoCu_{0.2}$. Insets are TEM images of corresponding Co-Cu samples.(e) Bright-field TEM image of $CoCu_{0.1}$ and (f-h) the corresponding element maps of Co (green) and Cu (red) in $CoCu_{0.01}$ nanocrystals.

The proposed formation mechanism of Co-Pd and Co-Cu nanocrysals with 1D structure was shown in Scheme 1. Firstly, the carbonyl of stearic acid and the amidogen of cetylamine showed a coordination effect with Co^{2+}, and this coordination effect reduced the concentration of Co^{2+} in the solution which made the coordination compound as a "reservoir" to control the concentration of Co^{2+} in the solution (Scheme 1a). As Pd or Cu has higher electronegativity than Co, a portion of Pd^{2+} or Cu^{2+} could be reduced preferentially to form Pd or Cu nuclei. The formation of Pd nuclei or Cu nuclei enhanced the reduction of Co^{2+} to Co by lowering the activity energy of this reduction process, resulting in the decomposition of the coordination compound to liberate Co^{2+} ions slowly (Scheme 1b). With the slow release of Co^{2+} from the "reservoir" as well as the reduction of Co^{2+} to Co, these Pd or Cu nuclei packed by more and more Co atoms grew slowly to form the cores of multipods. Meanwhile hexadecylamine and stearic acid liberated from "reservoir" also started to absorb on these growing cores (Scheme 1c). Surfactants like hexadecylamine and stearic acid can coordinate along the *c* axis of the *hcp* structure and make the (001) facets of *hcp* structured domains of the core exposed to the incoming cobalt atoms (Scheme 1d). The hexadecylamine and stearic acid continued to coordinate to the (101) crystal face of the *hcp* structure, where the grow occurred preferentially along (001) directions. Eventually, the dissolving, diffusion and deposition of Co in the reaction system evolved in to 1D nanostructure with the help of surfactants and prenucleated seeds (Scheme 1e).

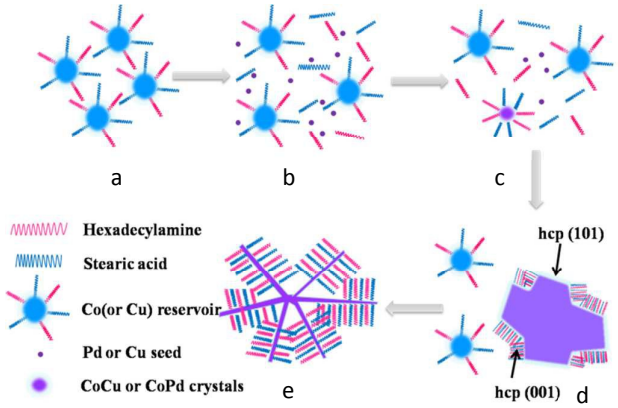

Scheme 1. The proposed formation mechanism of Co-Pd and Co-Cu nanocrysals with 1D structure.

The XRD studies show that as-synthesized Co-Pd nanocrystals are typically indexed as the (100), (002), (101), (102) and (110) diffractions, matching well with Co nanocrystals (Figure 3a). Diffraction peaks from $CoCu_{0.05}$ nanocrystals are similar to Co nanocrystals, but $CoCu_{0.1}$ and $CoCu_{0.2}$ made a difference show that (111) and (200) peaks (red triangle) located at 2θ = 43.5°and 50.6° correspond to cubic Cu phase (JCPDS No.04-0836). The surface areas of the Co-Pd and Co-Cu nanocrystals were determined from N_2 sorption measurements shown in Figure 3b. The surface areas, shown in Table S2, of Co-based nanocrystals with 1D branches are small. The electronic properties of Co, Co-Pd and Co-Cu

nanocrystals were studied by XPS, as presented in Figure 3c and Figure S6. The occurrence of satellite structure leads to the deconvolution of Co $2p_{1/2}$ and $2p_{3/2}$ excitations. The presence of Co^0, Co^{2+}, and Co^{3+} is in Co 2p spectra of all samples, while Co^{2+} dominates the surface of samples, demonstrating the existence of CoO. Co $2p_{3/2}$ electron binding energy of $CoPd_{0.01}$ is 1.0 eV higher than the value characteristic of $CoCu_{0.1}$ and the shift in binding energy reflects the fact that the effect of Pd on electronic properties of Co is bigger than that of Cu, suggesting that Co-Pd nanocrystals give rise to unusual catalysis. Cu 2p spectra could be found in Co-Cu nanocrystals, as shown in Figure 3d. Noted that the peak at 933.9 eV is assigned to Cu^{2+} and the peak at 933.2 eV is assigned to Cu/Cu^+, which indicates Cu^{2+} state dominates the surface of Co-Cu nanocrystals.

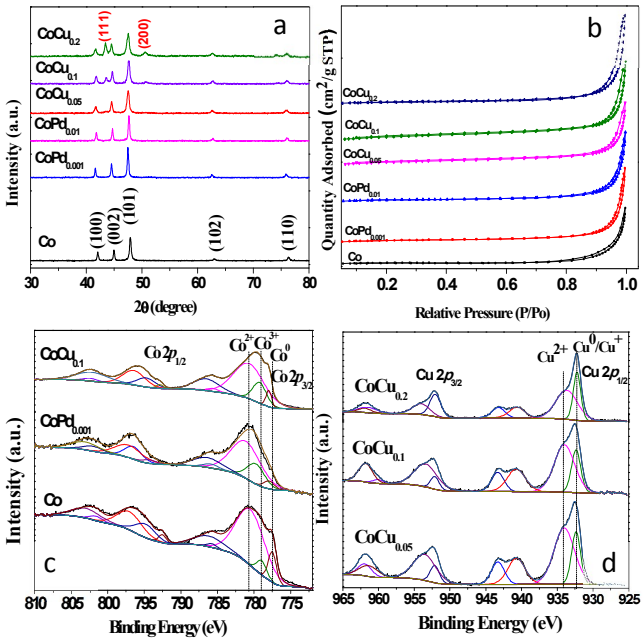

Figure 3. (a) XRD patterns of Co, $CoPd_{0.001}$, $CoPd_{0.01}$, $CoCu_{0.05}$, $CoCu_{0.1}$ and $CoCu_{0.2}$ nanocrystals. (b) Nitrogen absorption isotherms of Co, $CoPd_{0.001}$, $CoPd_{0.01}$, $CoCu_{0.05}$, $CoCu_{0.1}$ and $CoCu_{0.2}$ nanocrystals. (c) Co 2p electron region of XPS profiles of Co, $CoPd_{0.001}$ and $CoCu_{0.1}$ nanocrystals. (d) Cu 2p electron region of XPS profiles of $CoCu_{0.05}$, $CoCu_{0.1}$ and $CoCu_{0.2}$ nanocrystals.

Bimetallic Co-Pd and Co-Cu nanocrystals with 1D structure were evaluated to catalyze syngas conversion (Table S3-7). Co-Pd nanocrystals exhibited higher CO conversion and gave rise to lower CH_4 selectivity than Co-Cu nanocrystals (Figure 4a and Figure S7a). With temperature, the catalytic activity of these catalysts increased and especially $CoPd_{0.001}$ nanocrystals gave rise to 71.2 % CO conversion at 260 °C. Among the Co-Cu nanocrystals, $CoCu_{0.1}$ showed the highest CO conversion, compared to $CoCu_{0.05}$ and $CoCu_{0.2}$. Figure S7b-c indeed confirmed that Co-Pd nanocrystals gave much high selectivity towards hydrocarbons, while Co-Cu nanocrystals made a little high selectivity for alcohols. For all of these Co-based nanocrystals studied here, CO_2 selectivity is quite low over a range of temperatures (Figure S7d). Moreover, CO conversion over Co-Pd nanocrystals was higher than Co nanocrystals (the morphology of Co is shown in Figure S1a-b), revealing that appropriate Pd into Co nanocrystals can enhance hydrogenation activity of Co catalysts (Table S8). An intriguing observation is the high selective towards long-chain products over Co-Pd nanocrystals. From Anderson-Schulz-Flory (ASF) plots based on distribution of products over different catalysts (Figure S8), Co-Cu nanocrystals favor the formation of light products (C_1-C_8 hydrocarbons and C_1-C_5 alcohols), and Co-Pd nanocrystals favor the carbon chain growth to obtain heavy hydrocarbons (C_n, n>7). ASF chain-lengthening probabilities for products are up to 0.91 over $CoPd_{0.001}$.

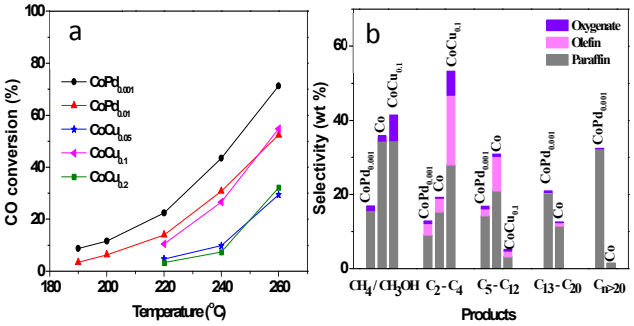

Figure 4. (a) Catalytic activity of Co-Pd and Co-Cu nanocrystals with 1D branches for selective hydrogenation of CO. (b) Product selectivity obtained over $CoPd_{0.001}$, $CoCu_{0.1}$ and Co nanocrystals, respectively (Selectivity is based on weight fraction of products collected on 220 °C).

For further realizing selective control on syngas conversion towards heavy paraffins, light olefins or alcohols via incorporating appropriate second metal on Co catalyst, in detail, we contrasted the catalysis of Co, $CoPd_{0.001}$ and $CoCu_{0.1}$ nanocrystals in different product range including C_1, C_2-C_4, C_5-C_{12}, C_{13}-C_{20}, and C_n>20 (Figure 4b). In C_1 composition (CH_4 and CH_3OH), $CoPd_{0.001}$ nanocrystals could achieve less undesirable CH_4/CH_3OH in comparison with Co and $CoCu_{0.1}$. For C_2-C_4 products (gases), $CoCu_{0.1}$ nanocrystals exhibited higher selectivity for light products including olefin, oxygenate and paraffin among these three catalysts. Although Co nanocrystals can give more gasoline (C_5-C_{12}), $CoPd_{0.001}$ nanocrystals can obtain more diesel (C_{13}-C_{20}). For $C_{n>20}$ product range (waxes), $CoPd_{0.001}$ nanocrystals gave rise to more wax products. Additionally, in C_2-C_{12} composition range, the ratio value of olefin to paraffin on $CoCu_{0.1}$ (0.66) is much higher than the values on Co (0.36) and $CoPd_{0.001}$ (0.22) , which infers that $CoCu_{0.1}$ nanocrystals can act as catalyst for more light olefins.

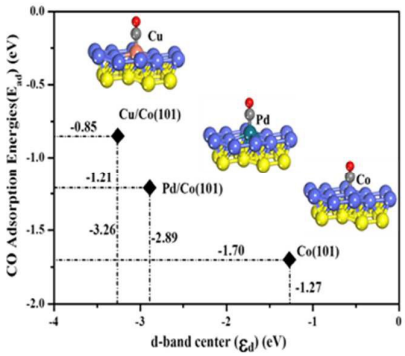

Figure 5. CO adsorption energies on the top sites of Co (101), Cu/Co (101) and Pd/Co (101) surface versus the d-band center. Here, a 8 layers with p(2×3) Co (101) supercell slab models was utilized and one surface Co on the step was substituted by a Pd or Cu atom. Adsorption and reaction were performed on one side of the exposed surface with substituted Pd or Cu atom. Each slab was separated by 13 Å of vacuum normal to the surface.

It is well known that oxygenates selectivity is controlled by the capabilities of catalysts to perform hydrogenation/dissociation/coupling of intermediate carbon species CH_x and C-C chain formation by CO/CHO insertion into CH_x.[21-23] To improve the selectivity of oxygenates, we need tune the relative activity of CO/CHO insertion into CH_x, that is, there must be a certain amount of CO kept on the surface for further insertion reaction without dissociation.[24] To provide a mechanistic understanding of selective control on syngas conversion over the experimentally observed Co-Pd and Co-Cu (101) surfaces, the corresponding CO adsorption energies versus the d-band center on the Cu/Co (101) and Pd/Co (101) surfaces were investigated by density functional theory calculation. Figure 5 reveals that the adsorption energy of CO at the top site on Pd/Co (101) surface (-1.21 eV) was 0.36 eV more exothermic than that on the Cu/Co(101) surface (-0.85 eV), indicating that CO diffusion on the Cu/Co(101) surface is easier than Pd/Co(101) surface. The calculated d-band center for the surface Cu and Pd atom on the two surface are -3.26 eV and -2.89 eV, respectively, as shown in Figure 5. The farther location of the d-band center (ε_d) relative to the Fermi level results in the weaker adsorption energy obtained in case of CO adsorption on the Cu/Co (101) surface, due to the closer d-band center to the Fermi level, the stronger the adsorption energy.[25] These energy data reveal the high mobility of CO on the Cu/Co (101) surface, therefore, it becomes possible to spot metal like Cu on the Co (101) surface to improve oxygenates formation.

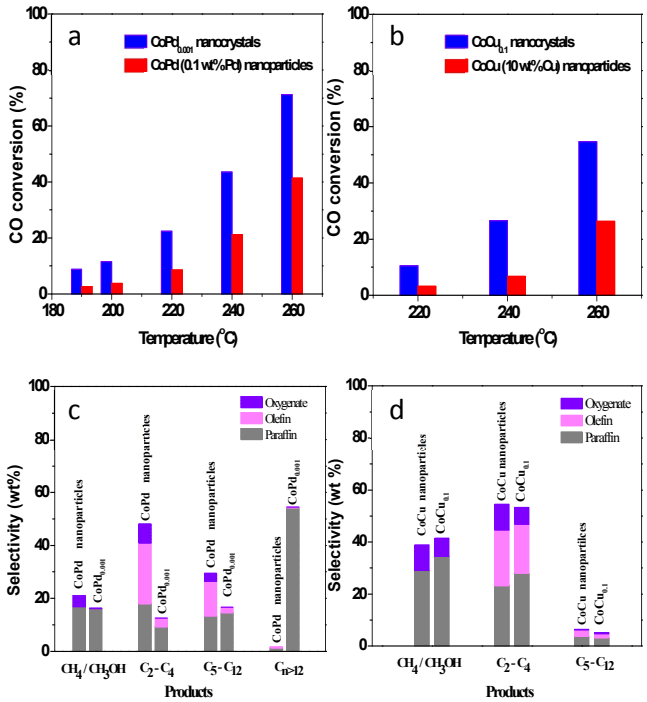

Figure 6. Comparison of catalytic activity for (a) $CoPd_{0.001}$ nanocrystals and CoPd (0.1 wt% Pd) nanoparticles and (b) $CoCu_{0.1}$ nanocrystals and CoCu (10 wt% Cu) nanoparticles. Comparison of products selectivity from syngas conversion over (c) $CoPd_{0.001}$ nanocrystals and CoPd (0.1wt% Pd) nanoparticles, and (d) $CoCu_{0.1}$ nanocrystals and CoCu (10 wt% Cu) nanoparticles (products were collected at 220 °C).

In contrast, conventional CoPd (0.1 wt% Pd) and CoCu (10 wt% Cu) nanoparticles were prepared using coprecipitation methods, and the morphology and surface areas of these nanoparticles were displayed in Figure S9. It is found, as shown in Figure 6a-b, that $CoPd_{0.001}$ and $CoCu_{0.1}$ nanocrystals with 1D structure are more effective than conventional CoPd (0.1 wt% Pd) and CoCu (10 wt% Cu) nanoparticles for the catalytic hydrogenation of CO, respectively. Figure S10a-b show that $CoPd_{0.001}$ and $CoCu_{0.1}$ exhibited enhanced catalytic activity per unit surface area for CO hydrogenation, as compared to conventional nanoparticles. An interesting feature emerges by comparing product selectivity of Co-based bimetallic nanocrystals with conventional nanoparticles. $CoPd_{0.001}$ nanocrystals can achieve more heavy hydrocarbons (C_n, n>12) than CoPd (0.1 wt% Pd) nanoparticles (Figure 6c), and ASF chain-lengthening probability for products over $CoPd_{0.001}$ nanocrystals (α=0.91) is higher than that over CoPd (0.1 wt% Pd) nanoparticles (α=0.62) (Figure S10c). However, $CoCu_{0.1}$ nanocrystals and CoCu (10 wt% Cu) nanoparticles were found to be similar catalytic selectivity for syngas conversion (Figure 6d). The different phenomena suggest that the catalytic selectivity of Co-based bimetallic catalysts is ascribed not only to the structure effect but also to the synergistic action of metals. It is also reflected by XPS studies, that is, Co 2p binding energy of $CoCu_{0.1}$ is similar with that of CoCu (10 wt% Cu) nanoparticles, whereas Co 2p electron binding energy of $CoPd_{0.001}$ is 1.2 eV higher than the value characteric of CoPd (0.1 wt% Pd) nanoparticles (Figue 7). It reflects that the effect of Pd on electronic properties of Co is related to the structure of CoPd, therefore the structure of CoPd catalysts determines their catalytic performance. The phenomena are inspiring and further study is in progress.

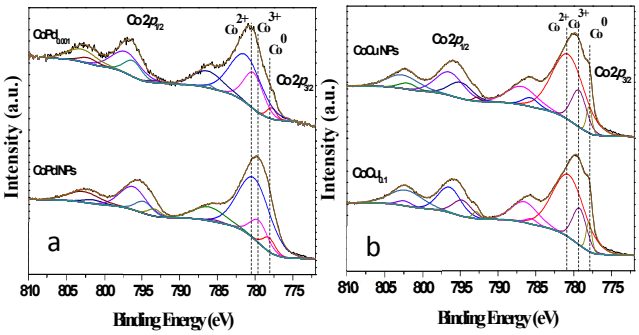

Figure 7. (a) Co 2p electron region of XPS spectra of $CoPd_{0.001}$ nanocrystals and CoPd (0.1 wt% Pd) nanoparticles. (b) Co 2p electron region of XPS spectra of $CoCu_{0.1}$ nanocrystals and CoCu (10 wt% Cu) nanoparticles. (Note: NPs: nanoparticles)

The 3D core-shell geometry of Co-based bimetallic nanocrystals appears to be robust during the catalytic processes.

The structure of Co-Cu nanocrystals has changed very little after catalytic reaction, though the core of Co-Pd became larger and the length of peripheral branches was shorter (Figure 8a-b and Figure S11a,f,g). Distribution of Pd and Co is still homogenous in spent Co-Pd nanocrystals (Figure S11b-e). The space distribution of elements of spent Co-Cu nanocrystals showed a similar vision to that of fresh ones, indicated by the element mapping (Figure 8c-f), where the concentration of Cu in the kernel is obvious higher than that on the periphery. The surface areas and lattice structure of these Co-based catalysts after catalytic tests were unchanged (Figure S12). However, XPS studies indicated that the surface composition of Co-Cu nanocrystals after catalytic reactions seems to reorganize, although the mobility of Co and Cu or Pd was not found by element mapping. The content of Cu on the surface of spent catalysts was lower than that of fresh ones (Table S1). The phenomenon might be ascribed to the segregation of Co and Cu, as well as the mobility of Co under syngas exposure, which is agreement with results of literature.[26] From Figure 9, the Co 2p spectra of spent $CoPd_{0.001}$ and $CoCu_{0.1}$ catalysts contain Co^0, Co^{2+} and Co^{3+}, however, the relative intensities of Co^0 is higher than those of fresh ones. Corresponding Cu 2p spectra of spent $CoCu_{0.1}$ are unchanged compared with those of fresh one (Figure S13). These results manifest the compositional reorganization of surface phases, and still call for a more in-situ spectroscopic investigation.

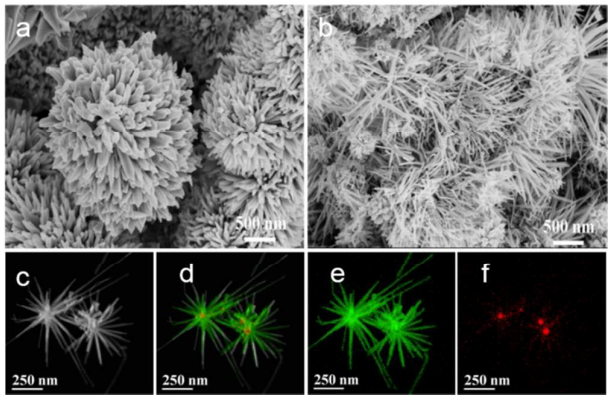

Figure 8. SEM images of (a) $CoPd_{0.001}$ and (b) $CoCu_{0.1}$ nanocrystals after catalytic tests. (c) Bright-field TEM image of $CoCu_{0.1}$ and (d-f) the corresponding element maps of Co (green) and Cu (red) in $CoCu_{0.1}$ nanocrystals after catalytic test (220 °C, 6 MP, 24 hr).

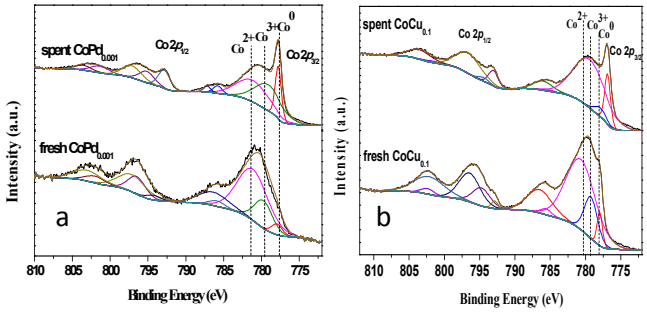

Figure 9. (a) Co 2p electron region of XPS profiles of fresh and spent $CoPd_{0.001}$. (b) Co 2p electron region of XPS profiles of fresh and spent $CoCu_{0.1}$.

Conclusions

In summary, robust Co-Pd and Co-Cu nanocrystals with 1D structure have been fabricated through a heterogeneous nucleation of Co atoms onto the prenucleated Pd or Cu seeds. By switching the prenucleated metal to form Co-Pd or Co-Cu nanocrystals, selectivity control on syngas conversion could be purposely adjusted towards light olefins, heavy paraffins or alcohols. Appropriate Pd incorporation into Co nanocrystals favors the carbon chain growth to obtain more long-chain hydrocarbons and appropriate Cu introduction into Co nanocrystals improves the selectivity of light olefins and oxygenates. Co-based bimetallic nanocrystals with 1D structure are more effective than the corresponding Co-based nanoparticles for CO hydrogenation. Selective control on catalytic reactions by switching second metal nucleated on one metal should aid in the design of bimetal nanocatalysts for specific reaction and the correlation their structure with properties.

Acknowledgements

We are grateful for financial support by National Natural Science Foundation of China (21273151, 21403277), Shanghai Pujiang Program (13PJ1407700), Shell Global Solutions International B. V. and Hundred Talent Program of CAS.

Notes and references

1. F. Fischer and H. Tropsch, *Brennst.-Chem.*, 1923, **4**, 276-285; F. Fischer, H. Tropsch, *Brennst.-Chem.,* 1926, **7**, 97-116.
2. K. G. Fang, D. B. Li, M. G. Lin, M. L. Xiang, W. Wei and Y. H. Sun, *Catal. Today,* 2009, **147**, 133-138.
3. Q. H. Zhong, J. C. Kang and Y. Wang, *ChemCatChem*, 2010, **2**, 1030-1058.
4. A. Y. Khodakov, W. Chu and P. Fongarland, *Chem. Rev.,* 2007, **107**, 1692-1744.
5. H. M. T. Galvis, J. H. Bitter, C. B. Khare, M. Ruitenbeek, A. I. Dugulan and K. P. de Jong, *Science*, 2012, **335**, 835-838.
6. Y. Z. Xiang, V. Chitry, P. Liddicoat, P. Felfer, J. Cairney, S. Ringer and N. Kruse, *J. Am. Chem. Soc.,* 2013, **135**, 7114-7117.
7. E. de. Smit and B. M. Weckhuysen, *Chem. Soc. Rev.*, 2008, **37**, 2758-2781.
8. P. Munnik, P. E. de Jongh and K. P. De Jong, *J. Am. Chem. Soc.*, 2014, **136**, 7333-7340.
9. K. Xiao, X. Z. Qi, Z. H. Bao, X. X. Wang, L. S. Zhong, K. G. Fang, M. G. Lin and Y. H. Sun, *Catal. Sci. Tech.,* 2013, **3**, 1591-1602.
10. T. Asefa, *ChemCatChem*., 2013, **5**, 1698-1700.
11. S. L. Sun and N. Tsubaki, K. Fujimoto, *Appl. Catal.,* 2000, **202**, 121-131.
12. M. Gupta, M. L. Smith and J. J. Spivey, *ACS Catal.*, 2011, **1**, 641–656.
13. Y. Z. Xiang, R. Barbosa and N. Kruse, *ACS Catal.,* 2014, **4**, 2792−2800.
14. V. R. Calderone, N. R. Shuji, D. C. Ferr and G. Rothenberg, *Green Chem.*, 2011, **13**, 1950-1959.
15. T. Teranishi, M. Saruyama, M. Nakaya and M. Kanehara, *Angew. Chem. Int. Ed.*, 2007, **46**, 1713-1715.
16. X. C. Ye, D. R. Hickey, J. Y. Fei, B. T. Diroll, T. Paik, J. J. Chen and C. B. Murray, *J. Am. Chem. Soc.,* 2014, **136**, 5106-5115.
17. R. S. Wagner and W. C. Ellis, *Appl. Phys. Lett.*, 1964, **4**, 89-90.
18. N, Tien-Thao, M. H. Zahedi-Niaki, H. Alamdari and S. J. Kaliaguine, *J. Catal.,* 2007, **245**, 348-357.

19. N. D. Subramanian, G. Balaji, C. S. S. R. Kumar and J. J. Spivey, *Catal. Today,* 2009, **147**, 100-106.
20. K. Xiao; Z. H. Bao, X. Z. Qi, X. X. Wang, L.S. Zhong, K. G. Fang, M. G. Lin and Y. H. Sun, *Chin. J. Catal.*, 2013, **34**, 116-129.
21. D. Lv, Y. Zhu and Y. H. Sun, *Chin. J. Catal.,* 2013, **34**, 1998-2003.
22. B. Hammer and J. K. Nørskov, *Adv. Catal.,* 2000, **45**, 71-129.
23. G. Prieto, S. Beijer, M. L. Smith, M. He, Y. Au, Z. Wang, A. D. Bruce, K. P. de Jong, J. J. Spivey and P. E. de Jongh, *Angew. Chem. Int. Ed.,* 2014, **53**, 6397-6401.
24. Y. H. Zhao, K. J. Sun, X. F. Ma, J. X. Liu, D. P. Sun, H. Y. Su and W. X. Li, *Angew. Chem. Int. Ed.,* 2011, **50**, 5335-5338.
25. B. Hammer and J. K. Nørskov, *Surf. Sci.*, 1995, **343**, 211-220.
26. S. Carenco, A. Tuxen, M. Chintapalli, E. Pach, C. Escudero, T. D. Ewers, P. Jiang, F. Borondics, G. Thornton, A. P. Alivisatos, H. Bluhm, J. H. Guo and M. Salmeron, *J. Phys. Chem. C.*, 2013, **117**, 6259-6266.